Surface-Induced Hybridization between Graphene and Titanium

Allen L. Hsu,[†,*] Roland J. Koch,[‡] Mitchell T. Ong,[§,∥] Wenjing Fang,[†] Mario Hofmann,[†] Ki Kang Kim,[†,⊥] Thomas Seyller,[‡] Mildred S. Dresselhaus,[†,#] Evan J. Reed,[§] Jing Kong,[†] and Tomás Palacios[†]

[†]Department of Electrical Engineering and Computer Sciences, Massachusetts Institute of Technology, Cambridge, Massachusetts 02139, United States, [‡]Institut für Physik, Technische Universität Chemnitz, 09126 Chemnitz, Germany, [§]Department of Materials Science and Engineering, Stanford University, Stanford, California 94305, United States, [∥]Condensed Matter and Materials Division, Physical and Life Sciences Directorate, Lawrence Livermore National Laboratory, Livermore, California 94550, United States, [⊥]Department of Energy and Materials Engineering, Dongguk University, Seoul 100-715, Republic of Korea, and [#]Department of Physics, Massachusetts Institute of Technology, Cambridge, Massachusetts 02139, United States

ABSTRACT Carbon-based materials such as graphene sheets and carbon nanotubes have inspired a broad range of applications ranging from high-speed flexible electronics all the way to ultrastrong membranes. However, many of these applications are limited by the complex interactions between carbon-based materials and metals. In this work, we experimentally investigate the structural interactions between graphene and transition metals such as palladium (Pd) and titanium (Ti), which have been confirmed by density functional simulations. We find that the adsorption of titanium on graphene is more energetically favorable than in the case of most metals, and density functional theory shows that a surface induced p−d hybridization occurs between atomic carbon and titanium orbitals. This strong affinity between the two materials results in a short-range ordered crystalline deposition on top of graphene as well as chemical modifications to graphene as seen by Raman and X-ray photoemission spectroscopy (XPS). This induced hybridization is interface-specific and has major consequences for contacting graphene−nanoelectronic devices as well as applications toward metal-induced chemical functionalization of graphene.

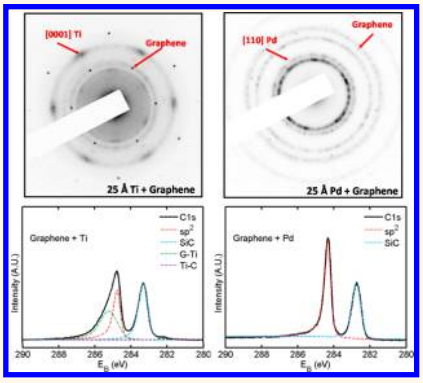

KEYWORDS: graphene · titanium · Raman spectroscopy · chemical functionalization · density functional theory · hybridization

Graphene is a two-dimensional carbon-based material with amazing intrinsic properties including ultrahigh carrier mobility (>100000 $cm^2 V^{-1} s^{-1}$),[1] thermal conductivity (5×10^3 W $m^{-1} K^{-1}$),[2] mechanical strength (42 N/m),[3] and chemical resistance.[4] While these intrinsic properties have inspired many graphene applications,[5−11] graphene's actual performance is often limited by its extrinsic interactions with nearby surfaces.[12−14] One of the most critical interfaces is that between graphene and a metal. These interactions are not only important for high-frequency RF electronics—many other applications such as spintronic devices,[15] ultrathin catalysts,[16] growth templates,[17] *etc.* all rely on graphene−metal interactions. Furthermore, as people look toward modifying and engineering graphene's properties,[18−21] previous *in situ* angle resolved photoemission spectroscopy (ARPES) revealed drastic changes in graphene's linear band structure when epitaxial graphene is synthesized directly on a single-crystal transition-metal substrate such as Ni, Ir, and Ru.[22−27] Furthermore, changes in graphene's work function by the deposition of various metals (Au, Ni, Co, *etc.*)[28,29] were observed. However, there is still much unknown about the structure and the impact to carrier transport that these various metals have on graphene.[30]

In this investigation, we utilize Raman spectroscopy to identify a surface-induced scattering term between graphene and a transition metal—titanium. This new scattering term drastically modifies graphene's Raman spectra by quenching the double-resonant (2D) process. This quenching is believed to be caused by a surface-induced chemical modification, shown by X-ray photoemission spectroscopy (XPS), as well as a strong epitaxial ordering between graphene and titanium, shown through transmission electron microscopy (TEM). This chemical modification is entirely surface-dominated

* Address correspondence to allenhsu@mit.edu.

Received for review December 24, 2013 and accepted July 17, 2014.

Published online July 17, 2014
10.1021/nn502842x

and completely reversible. For comparison, we also investigated the interaction between graphene and palladium using XPS and Raman. Furthermore, simulations utilizing density functional theory (DFT) show that the electronic hybridization between the titanium p−d orbitals and the large binding energy between graphene and titanium explain the microscopic origins of this chemical modification. These results not only illuminate future routes for improving ohmic contact technology for carbon nanoelectronics but also might lead toward the chemical modification of graphene's electronic structure as well. Finally, the crystalline Ti template on top of graphene may also serve as an epitaxial buffer for the integration of other materials with graphene.[31]

RESULTS

Raman Spectroscopy. Probing the electronic properties of graphene in contact with metals by optical techniques, such as Raman spectroscopy, provides a unique opportunity to selectively monitor the graphene quality through a thin metal film.[29] For Raman spectroscopy, we utilize copper-grown CVD graphene transferred onto thermally grown SiO_2 followed by a forming gas anneal to ensure a clean graphene interface.[32] Next, we deposit an optically thin layer (25 Å) of different metals (Ti, Pd, Au, or Ni) onto separate graphene samples (1 Å/s), using a shadow mask to create a thickness profile. After deposition, the samples are measured *ex situ* in a Raman microscope with a 532 nm laser light source. Figure 1 shows the resulting Raman spectra for the various graphene−metal combinations (a) as well as the experimental schematic of the measurement (b). The data for most of the metals (Au, Ni, and Pd) agrees well with previous reports in the literature.[28,29,33] However, what has not been reported before is the drastic quenching of the D and 2D peaks and the strong down shift of the G peak to ∼1560−1570 cm^{-1} after titanium deposition. Furthermore, while the 2D peak is completely absent in our sample, other Raman features such as the silicon substrate or G peak of the graphene are still observable, discounting electromagnetic shielding effects by the metal films (Supporting Information, Figure S1). Some previous reports have shown an increased D peak due to titanium,[34] but our spectra for titanium on graphene show no experimentally identifiable D peak. The data across various regions, and thus across various film thicknesses, shows a ratio of the 2D peak position/G peak position of ∼2 (black line Figure 1c). This indicates strained graphene.[35] Unfortunately, for the titanium sample, there is no 2D peak to be found; thus, the random distribution of points along the *y*-axis is the result of the noise in the peak value of the background signal. The data along the *x*-axis shows a clustering of the G peak position around 1570 cm^{-1}, which is much lower than other metals.

Assuming this effect originates between graphene and metallic titanium, we ran further experiments to rule out artificial effects caused by (1) (hydro)-carbon residues from transfer, (2) oxidized titanium, and (3) destruction of the intrinsic graphene lattice. To address

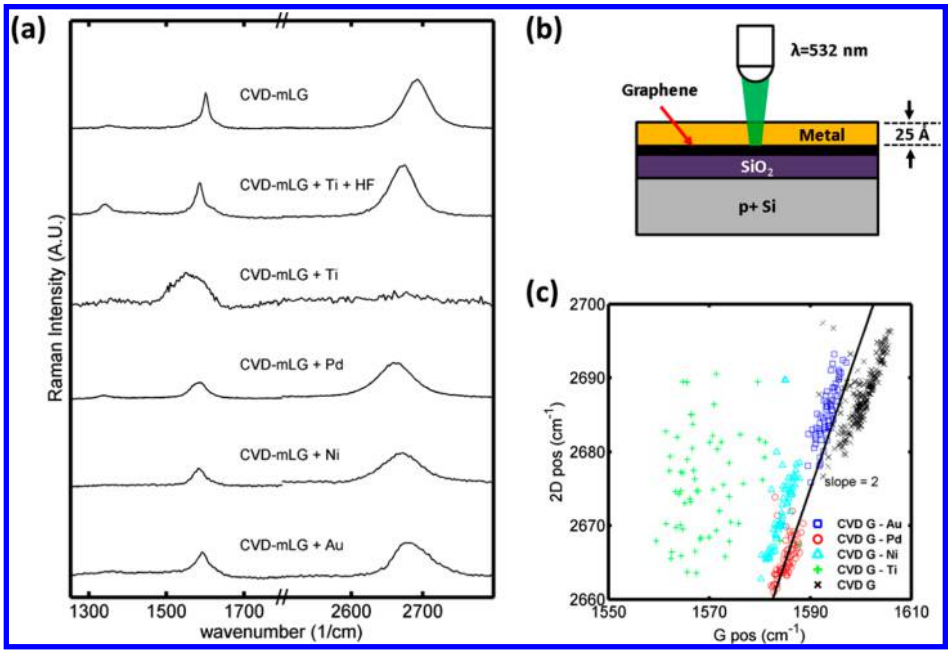

Figure 1. Raman spectroscopy of graphene underneath evaporated metal. (a) Raman spectra of graphene before and after various metals (25 Å of Au, Ni, Ti, or Pd) are evaporated on top. (b) Schematic of the sample during measurement. Raman laser excitation is done at λ= 532 nm. (c) Plot of the fitted 2D peak position versus G position for the various metals deposited. Due to the absent 2D peak in the titanium data, the 2D peak position is simply represented by the peak intensity position found in the background noise of the spectra. The black solid line represents expected strain effect on 2D peak position versus G position.

possible carbon residues after transfer, we repeated our Raman experiment utilizing other transfer techniques such as mechanical exfoliation of highly oriented pyrolytic graphene (HOPG) as well as direct synthesis of quasi-free-standing monolayer graphene on SiC (for detailed sample preparation procedures see the Methods). All samples showed the same drastic quenching of the 2D peak when titanium was deposited (Figure S2, Supporting Information). In addition, we also found that this effect could be purposely inhibited by introducing carbon residues at the surface (i.e., residues resulting from the exposure and development of a photoresist[36]). After discounting any effects due to carbon contamination, we next turned our attention to any possible titanium−oxygen effects at the interface. Since titanium naturally oxidizes upon exposure to air, we examined the Raman spectra of 5 Å of titanium (fully oxidized) on top of graphene and also found no observed quenching of the 2D peak (Figure S3a, Supporting Information). Consequently, this Raman effect is not the product of oxidized titanium at the graphene interface, supporting our assumption that upon *ex situ* Raman and oxidation of the titanium film the titanium in contact with the graphene is still metallic. However, this does mean that the thickness of the actual metallic titanium (*ex situ*) is perhaps less than the originally stated 25 Å due to a surface of insulating titanium oxide. Finally, to ensure that the graphene is still intact after deposition, we also measured the Raman spectra after the removal of the titanium by hydrofluoric acid (HF) in Figure 1a. The resulting spectra clearly shows that the G and 2D line shapes can be recovered after HF acid treatment, thus suggesting the titanium is not covalently bound to the graphene. There is, however, a small D peak present after etching that could be due to damage through either the delamination of the graphene from the underlying SiO_2 or possibly some direct etching of graphene at defects or grain boundaries. In either case, the graphene's lattice has not been completely destroyed by the titanium deposition, indicating that the surface interaction between the two materials interferes with the double-resonant Raman process.

The intensity of the 2D peak gives important information about the charge carrier dynamics in graphene. Assuming a Lorentzian line shape for the 2D peak, the intensity is directly proportional to the charge carrier lifetime (γ_{2D}), which can be separated into two components: (1) the intrinsic electron phonon lifetime ($\gamma_{(e\text{-}ph)}$) and (2) the electron-defect lifetime ($\gamma_{(defect)}$) shown in eq 1.

$$\gamma_{2D} = \gamma_{(e\text{-}ph)} + \gamma_{(defect)} \quad (1)$$

Previous studies[37,38] investigated how $\gamma_{(e\text{-}ph)}$ is decreased by doping, similar to graphite-intercalation compounds (GIC). Their explanations always rely on a strong difference in the work function between graphite/graphene and the intercalation material. However, for titanium and graphene the work function is almost the same. Consequently, these observations cannot explain our results.[39] A different study conducted by Mauri *et al*[40] ascribing lifetime broadening effects ($\gamma_{(defect)}$) to defects, such as charged impurity scattering, on-site, and hopping defects, appear more plausible between graphene and titanium. Utilizing a model system of amorphous carbon, they found that at low defect concentrations $\gamma_{(e\text{-}ph)}$ dominates γ_{2D}, and moreover, the intensity of the D peak is linearly dependent on the defect concentration. However, for large defect densities ($N_d > 10^{12}$ cm^{-2}) the intensities of the D and 2D peak eventually become inversely proportional with respect to defect density. This explains in part the lack of both a clearly defined D and 2D peak in the Raman spectra of amorphous carbon.[41−43] As this situation is very similar to our Raman experiments between graphene and titanium, the nature of potential lattice defects and disorder is less clear. We have shown that no significant structural damage is induced in the graphene by the HF-etching experiment. Furthermore, the line shape of the observed G peak is significantly broadened, consistent with an increased scattering term similar to amorphous carbon.[44] This is different from other previous works which have shown disruptions of the 2D peak of graphene on Pt substrates; however, they see almost no modification of the G peak line shape. Therefore, we propose that the metallic titanium deposited on top of graphene induces an entirely surface-mediated scattering term to the charge carriers within the graphene.

Atomic Force Microscopy. To verify the validity of this model, additional experiments were performed to clarify if this surface-induced scattering is either structural and/or chemical in nature. We use palladium deposited on top of graphene as a point of comparison for the titanium interaction. The structural nature of the graphene/titanium interaction was investigated using *ex situ* atomic force microscopy (AFM) and transmission electron microscopy (TEM). Parts a and b of Figure 2 show the AFM scans taken over a 5 μm × 5 μm scan region. The mean average surface roughness (R_a) of the titanium deposited onto graphene is almost indistinguishable from that of intrinsic graphene ($R_a \approx$ 0.18−0.25 nm). In contrast, palladium on graphene shows a much larger surface roughness ($R_a \sim 0.63$ nm), indicating a strong clustering and a Volmer−Weber growth mode (Figure S5, Supporting Information). However, at titanium films thicker than 10 nm, large hillocks begin to appear (>50 nm), as shown in Figure 2c. The stresses of the Ti film cause a buckling or delamination of the film from the substrate. This delamination is attributed to the weak adhesion energy between the transferred CVD graphene and the SiO_2 substrate (Supporting Information), but the external stresses caused by the Ti may also explain the

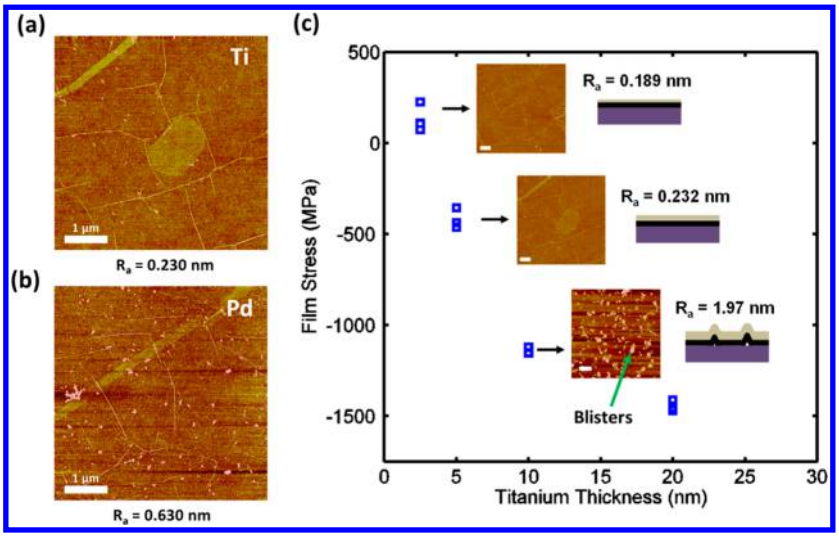

Figure 2. Investigating graphene wettability using atomic force microscopy (AFM). Images taken over a 5 μm × 5 μm scan area: (a) 25 Å of titanium evaporated on top of graphene; (b) 25 Å of palladium evaporated on top of graphene; (c) film stress (MPa) versus thickness of titanium. Inset: AFM of titanium at various thicknesses of titanium (25, 50, and 100 Å). Large hillocks or blisters (>30 nm) are observed after 100 Å of deposited titanium.

large downshift of the G-peak observed in Figure 1c. The stress of thicker deposited Pd (~50 nm), on the other hand, was measured to be significantly lower (<500 MPa).

Transmission Electron Microscopy. Utilizing selected area electron diffraction (SAED), we also identify the crystal orientation and structure between these metals and graphene. For this investigation, first graphene films were transferred and suspended onto TEM grids. Second, 2.5 nm of Ti or Pd was evaporated onto the already suspended graphene. These samples were then transferred *ex situ* to a TEM. Details of transfer technique are included in the Methods. The total sampling area from SAED is approximately 100 nm. Figure 3a shows the electron diffraction pattern for graphene (red) and titanium (white). The diffuse diffraction arcs correspond to a hexagonal closely packed (hcp) Ti lattice with a lattice constant ratio a_{Ti}/a_G = 1.19 (ideal = 1.199). The titanium lattice shows a distinct epitaxial ordering or alignment to the underlying graphene surface across the entire TEM sample. High-resolution (HR)TEM also shows a clear crystal structure to the titanium (Supporting Information, Figure S4), further supporting our assumption that the titanium at the graphene interface still remains metallic, even after the *ex situ* transfer to the TEM. Moreover, it shows a uniform coverage of titanium on top of graphene (Figure S5, Supporting Information). The palladium diffraction pattern in Figure 3b, on the other hand, shows many randomly oriented Pd clusters (4−5 nm in size) on the graphene surface (Figure S5, Supporting Information). By comparing the distance of the Pd diffraction rings it is possible to determine the vertical crystal orientation of the Pd clusters. Surprisingly, they are oriented in the [011] orientation of the face-centered-cubic (fcc) lattice. Moreover, it is possible to determine the lattice constant ratio between the palladium and the graphene to be a_{Pd}/a_G = 1.61, which is slightly larger than the ideal value of a_{Pd}/a_G = 1.59. This lattice orientation is unexpected as most simulations predict a [111] orientation between many fcc lattices such as palladium and the hexagonal surface of graphene.[45] This same orientation is also observed in our experiments for Au and Ni (Supporting Information, Figure S6). Parts c and d of Figure 3 show diagrams of the topography of the deposited metal films and the orientation relative to the graphene crystal lattice. The epitaxial orientation of the titanium suggests that the metal atoms are depositing onto the surface as well-ordered crystals with an average rotational alignment of 30° relative to the graphene crystal structure, whereas the Pd appears to be deposited in well-ordered clusters with a random orientation with respect to the graphene surface. The distinct epitaxy and stronger wettability between graphene and titanium, as compared to Pd, suggests a stronger interaction between the two.

X-ray Photoemission Spectroscopy. Now the question arises whether this epitaxy between titanium and graphene leads to a chemical modification of the underlying graphene? To clarify this aspect, we performed *in situ* deposition of titanium or palladium, with parallel acquisition of X-ray photoemission spectra (XPS) on epitaxial quasi-free-standing monolayer graphene (QFMLG) grown on SiC. This graphene substrate was chosen to ensure an *in situ* clean graphene surface by avoiding any transfer processes.[46] Contaminations from the *ex situ* transfer of the samples to the XPS chamber were removed by annealing the sample at 300 °C in a chamber with a base pressure better than 1 × 10^{-10} Torr for 5 min (for more details, see the Methods). The C 1s peak of the pristine sample is plotted in Figure 4a. The XPS spectrum shows two

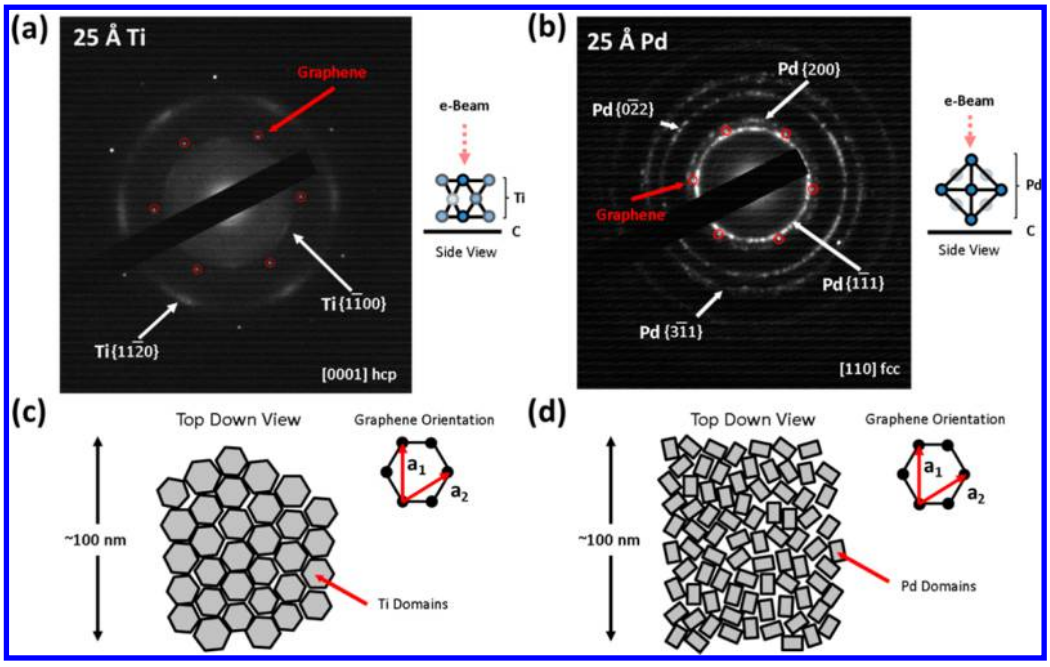

Figure 3. Selected area diffraction patterns using transmission electron microscopy (TEM). (a) Graphene/Ti (25 Å) showing a measured lattice constant ratio between a_{Ti}/a_G = 1.19. Red circles indicate graphene's first-order diffraction spots. The white arrows indicate titanium's diffraction spots. The zone axis of the electron beam [0001] and crystal orientation (hcp) is labeled in the lower right-hand corner. (b) Graphene/Pd (25 Å) showing a measured lattice constant ratio between a_{Pd}/a_G is 1.61. Unlike titanium where an epitaxial relation can be identified, the random orientation of the palladium domains results in diffraction spots arranged in a series of rings, which are also labeled by white arrows. Diagrams of the electron beam orientation relative to the crystal orientation of the metal are included alongside (a) and (b). (c) Diagram of a schematic of the orientation between titanium domains (domain shown schematically as a hexagon). A finite angular dispersion is included in the diagram due to the broadening of the diffraction spots in (a). The titanium domains are mainly oriented 30° relative to the graphene with a finite angular dispersion of ± <5°. while Figure (d) shows the formation of small nanodomains of randomly distributed Pd rotated around the [011] zone axis (domain shown schematically as a rectangle). Note domain sizes are not drawn to scale.

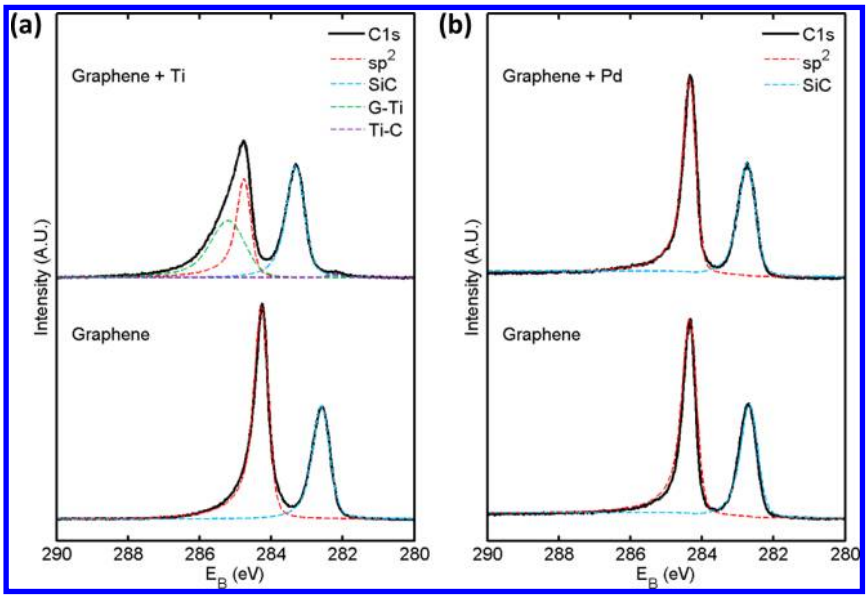

Figure 4. In situ synchrotron X-ray photoemission spectroscopy (XPS) spectra for the C 1s core level taken at a photon energy of 600 eV: (a) pristine quasi-freestanding graphene (QFMLG) on SiC(0001) (bottom), the carbon chemistry is divided into two peaks (1) sp^2-bonded carbon due to graphene (red) and the carbon bonded to silicon (light blue) from the substrate and in situ XPS of 2 ML of Ti evaporated on QFMLG. The carbon bonded in graphene undergoes a chemical modification shown by the arrow which is labeled in green (G-Ti). A small Ti−C peak at ~282 eV also appears in purple, while the substrate intensity does not change. (b) Pristine graphene shown in bottom and on top in situ XPS of 1.2 ML Pd evaporated on QFMLG.

distinct carbon chemistries: (1) the sp^2-bonded carbon from the graphene (E_B = 284.3 eV, fitted using a Doniach−Sunjic line shape) and (2) the chemistry of the SiC substrate (E_B = 282.6 eV, fitted using a Voigt line

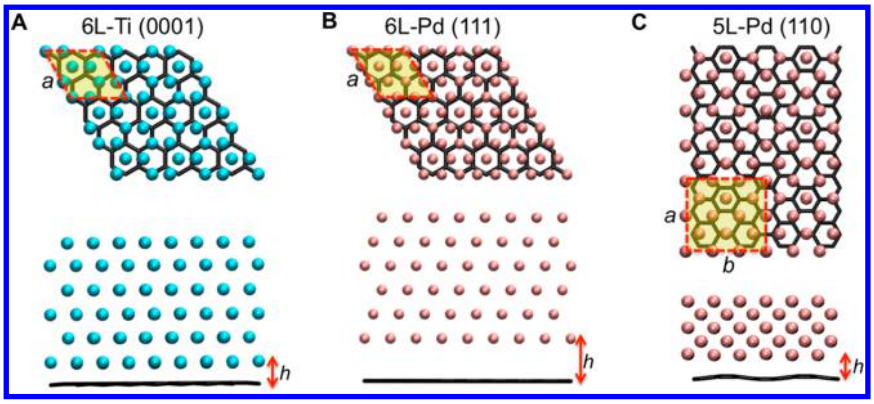

Figure 5. Density functional theory simulation of optimized equilibrium geometries. Top-down and side views of (a) 6-layer Ti(0001) on graphene, (b) 6-layer Pd(111), and (c) 5-layer Pd(110) on graphene. The primitive cell is highlighted in yellow. The equilibrium separation between the metals and graphene is represented by *h*. The dimensions of the unit cell are represented by *a* and *b*. For Ti(0001) and Pd(111), *a* = *b*, unlike the rectangular unit cell of Pd(110).

shape). As reported by Riedl *et al.*[46] and Speck *et al.*[47] no interface layer contribution is observed in the C 1s core level confirming we have only a monolayer of graphene. After the deposition of two monolayers (ML) of titanium (details of the deposition are explained in the Methods), we find that the C 1s peak undergoes a chemical modification. The graphene peak is now split into two contributions; 54% of the graphene peak is now shifted to a binding energy (E_B) of 285.2 eV. Furthermore, this new contributions is substantially broadened (fwhm ~0.8 eV). Moreover, we observe a very small amount of TiC (E_B = 282.2 eV) during the evaporation. This TiC component increases with evaporated titanium thickness, whereas the modified graphene component is attenuated with the same rate as the graphene and silicon carbide contributions during evaporation. Therefore, in contrast to other reports in the literature such as that of Gong *et al.*,[48] we can attribute the TiC to contamination of titanium from residual gas during and after the evaporation. Furthermore, the oxygen content within the film is also quite low as compared to a completely oxidized titanium film on graphene (Methods and Supporting Information, Figure S7b). After oxidation of the titanium film, the XPS spectrum of the C 1s almost returns to its pristine shape (Supporting Information, Figure S7a) suggesting a decoupling of the titanium from the graphene, which is consistent with our Raman experiments. Repeating the same experiment utilizing Pd, shown in Figure 4c, the sp^2 content of the graphene is completely preserved after the deposition of 1.2 ML Pd. Given the large density of carbon that has been modified by the titanium, this is well within a regime where the perturbation to the electronic lattice can suppress both the formation of a D and 2D peak in the Raman spectra of graphene.

DISCUSSION

Density Functional Theory. To investigate the origin of this surface induced chemical modification, we utilize density functional theory (DFT) simulations with Perdew–Burke–Ernzerhof (PBE) semilocal exchange and correlation[49] to compare the interaction between Pd and Ti (see the DFT simulation details). The supercell arrangements for Ti/graphene and Pd/graphene are shown in Figure 5a–c. For Pd/graphene, two orientations are considered, Pd(111) (Figure 5b) and Pd (110) (Figure 5c), in order to compare the observed Pd structures in TEM with previous simulations results.[39,45] The adsorption energies (E_{ads}) for each of the structures in Figure 5 are calculated using the expression

$$E_{ads} = E_{graph+metal} - E_{graph} - E_{metal} \quad (2)$$

Here, $E_{graph+metal}$ is the total energy for the graphene–metal complex, E_{graph} is the total energy of graphene, and E_{metal} is the total energy of the metal slab. These energies correspond to the optimized lattice parameters of minimal stress for each of the structures. As shown in Table 1, the adsorption energy between Ti(0001) and the graphene lattice is negative, while E_{ads} for Pd(111) on graphene is near zero. Furthermore, we can see that the Pd(110) case is 0.02 eV per C atom lower in energy than the (111) case, consistent with our TEM observations. The observed trends in the adsorption energies and graphene-metal distance (*h*) are in agreement with previous DFT calculations performed using the local-density approximation (LDA) exchange correlation functional as well as our AFM and TEM measurements.[39,45] Since the adsorption energy of Ti on graphene is negative for the (0001) configuration, it is energetically favorable for Ti atoms to completely wet the surface of graphene in a uniform fashion, consistent with experimental results.[50] For Pd, the adsorption energies in both orientations are near zero, suggesting a very weak driving force for forming an ordered system. However, the energy resolution of our calculations may not be high enough to confidently predict the nature of Pd on the surface. The side profile of Pd(110) on graphene in Figure 5c shows that the graphene sheet exhibits an out of plane curvature.

TABLE 1. Calculated Adsorption Energies (E_{ads}), Height above Graphene Surface (h), and % Strain on Metal and Graphene for 6L−Ti(0001), 6L−Pd(111), and 5L−Pd(110) on Graphene (a_{lat}, b_{lat})

	E_{ads} (eV/C atom)	h (Å)	% strain a_{lat} (graphene)	% strain a_{lat} (metal)	% strain b_{lat} (graphene)	% strain b_{lat} (metal)
6L−Ti(0001)	−0.258	2.08	2.00	−0.55		
6L−Pd(111)	0.014	4.04	−1.05	1.20		
5L−Pd(110)	−0.003	2.50	−0.24	2.31	0.62	−3.88

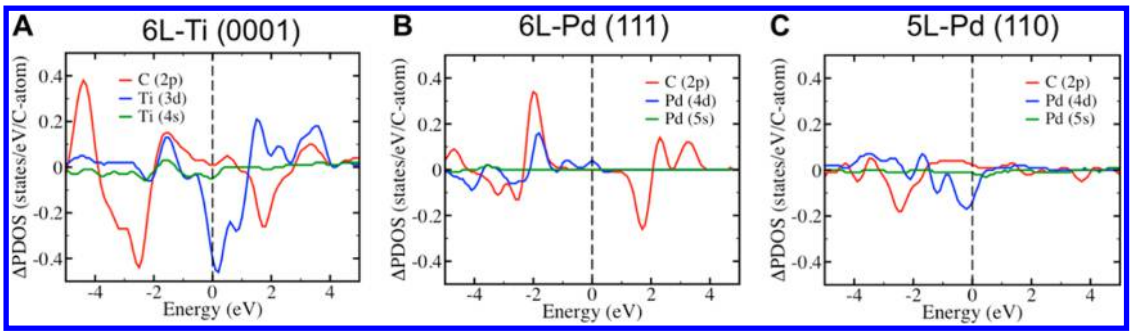

Figure 6. Difference between the projected density of states (PDOS) of interacting and isolated configurations indicating the contributions of individual p and d atomic orbitals near the Fermi level for (a) 6-layer Ti(0001), (b) 6-layer Pd(111), and 5-layer Pd(110) on graphene. Atomic orbital contributions from the metal are computed only for the metal layer adjacent to graphene.

While simulations for computationally tractability assumed a periodic supercell, the level of strain is sufficiently large enough that this configuration is unlikely to exist over many unit cells of graphene; possibly related to our observations from TEM that many small Pd clusters are observed (higher order corrections and van der Waals corrections included in Figure S8, Supporting Information). Figure 5 and Table 1 also show that the equilibrium distance between titanium and graphene is much closer than that of Pd and graphene, consistent with our model that the close proximity of the titanium atoms with graphene might be perturbing the electrons in the system.

The chemical modification to the electronic structure of graphene is shown in the calculated change in the projected density of states (ΔPDOS) (Figure 6). Here, we consider only the metal atoms in the first layer and the graphene sheet in the calculation of ΔPDOS. We observe in the chemical bonding a small increase in the p character from the graphene and a large decrease in the d character from the metal near the Fermi energy (between −1 and +1 eV) for 6L−Ti(0001). Therefore, the change in the valence p-orbital characteristics of graphene is consistent with our observed chemical modification to the inner core electrons as seen by XPS (Figure 4b). For the relevant case as seen by SAED (5L−Pd(110)), the ΔPDOS is much less significant than compared to both the 6L−Pd(111) and 6L−Ti(0001). While there is some mixing of states at the Fermi energy level for 5L−-Pd(110), we have assumed an ideal coating of Pd(110) on top of graphene, which is unlikely from our HR-TEM and AFM due to the poor wettability. Therefore, while Pd and G may have some p−d hybridization, any experimental quantity which would probe large areas (Raman, XPS, *etc.*) may be mitigated due to the small effective contact area between the evaporated Pd and graphene.

CONCLUSION

In conclusion, our modified Raman spectra of titanium on graphene is caused by a surface-induced scattering term resulting from both the small equilibrium distance between the two as well as a chemical p−d hybridization between the carbon and the titanium. This has important implications in the field of metal−graphene nanoelectronics. Currently, as all standard FET devices shrink in accordance with Moore's law, parasitic resistances due to contact resistances are actually much larger limiting factors than the intrinsic material itself.[51] Unlike contacting a 2D electron gas, the entire channel material is self-contained within the graphene itself. By observing both the structural nature of Ti and Pd on top of graphene as well as the chemical modification to graphene by these metals, one can gain more insight into improving graphene−metal contacts. The surface-induced scattering term, deduced from the 2D Raman peak, suggests that an electron scatters faster with the titanium-induced perturbation than with an optical phonon. This can drastically limit the charge carrier velocity underneath the contacts. On the other hand, other metals such as Pd may have a limited effective contact area due to the weak interaction to the graphene. However, besides ohmic contacts to graphene, this surface-induced hybridization of graphene with d-orbitals also opens up a new route of chemically modifying graphene. Where traditional work has shown

that metals can dope graphene, the strong adsorption energy between titanium and graphene could open new routes for chemically modifying graphene following work from organotitanium chemistries.[52] In the scope of previous studies on the chlorination and fluorination of graphene,[53,54] our work suggests that p−d hybridization from metal adsorbents could also serve as a valid possibility. In addition, by combining lithography techniques, this new metal-functionalization of graphene and the crystallinity of the titanium surface structure may even serve as a patterned growth template for the preparation of future nanomaterials.[55]

METHODS

Material Growth and Transfer and Preparation. *Graphene Growth Procedure.* Graphene was synthesized by low-pressure chemical vapor deposition using a copper foil (25 μm, Alfa Aesar) as a catalytic metal substrate. Before graphene growth, the copper foil was annealed at 1000 °C for 30 min under a 10 sccm hydrogen atmosphere (~330 mTorr) to increase the grain size and to ensure the growth of a smooth surface, followed by synthesizing graphene under 15 and 50 sccm of methane and hydrogen atmosphere for 40 min (~1.5 Torr) while maintaining the same temperature. During the cooling of the chamber, 10 sccm of hydrogen was flowed until room temperature was reached.

Transfer. Poly(methyl methacrylate) (PMMA) (4.5% in anisole) was spun on the graphene on copper foil with 2500 rpm for 1 min, followed by etching with copper etchant (CE-100, Transene). The film of PMMA/G was washed by DI water to remove the residual copper etchant. To remove the residual iron particles which came from the copper etchant ($FeCl_3$), the film was floated on 10% HCl for 20 min, followed by neutralization with deionized water. After the PMMA/G film was transferred onto either SiO_2/Si or a Quantifoil TEM grid (2.5 μm hole, Tel Pella), PMMA was removed by acetone vapor and thermal annealing at 450 °C for 2 h under an H_2/Ar atmosphere. In addition to thermally annealed samples, reference samples for TEM were also transferred without PMMA utilizing direct transfer of CVD graphene onto lacey carbon TEM grids.[56] Comparisons between these two techniques are included in the Supporting Information (Figure S9).

Metal Deposition and Sample Preparation. Pd, Ni, and Au were deposited by electron beam evaporator (Temescal) at a base pressure $<10^{-6}$ Torr room temperature. For titanium, the overnight pumping and predeposition of Ti lowered the base pressure to $\sim10^{-8}$ before the actual deposition on the sample. Deposition rates for all materials were kept at 1 Å/s. Shadow masking was done on all samples to provide an intrinsic reference.

Characterization. Raman line scans were performed in a home-built Raman system with a X−Y motorized microscope stage taken with a Nd:YAG laser at 532 nm at a power of ~1−2 mW using a 100× objective with a beam spot size of ~1 μm. Data was then processed with automated Lorentzian fitting in MATLAB. Selected area diffraction patterns were then taken using a JEOL 2010 transmission electron microscope at 80 kV. The surface morphology of the graphene and metal was examined by atomic force microscopy (Dimension 3100, Veeco). Stress measurements were then made using a KLA Tencor FLX 2320 on titanium deposited on top of standard silicon prime wafers. High-resolution TEM pictures of titanium on graphene are included in the Supporting Information (Figure S6).

Titanium Etching. Titanium was etched using a diluted HF (100:1) for 5 s.

XPS Characterization and QF-SiC Sample Preparation. Quasi-freestanding graphene on silicon carbide was grown by intercalating the buffer layer on a 6H−SiC(0001) surface with ultrapure molecular hydrogen using the same process in the same experimental setup previously published by Speck *et al.*[47] The buffer layer, which is a graphene layer covalently bound to the SiC surface, was grown by annealing the sample under argon atmosphere in an inductively heated oven at 1400 °C.[57] The buffer layer was checked to be free of graphene by using XPS, which ensures that after intercalation the sample is free of bilayer regions (Figure S10, Supporting Information). After transfer to a ultrahigh vacuum chamber used for photoelectron spectroscopy, the samples were annealed at 300 °C for 5 min to remove possible contaminations from the graphene surface. Titanium and palladium deposition were performed inside the ultrahigh vacuum (UHV) chamber using electron-beam evaporation from a rod at a deposition rate of 0.1 Å/min for Ti and 0.85 Å/min for Pd. The pressure during evaporation was kept below 2×10^{-10} Torr. Oxidation of the titanium was achieved by exposing the sample to 600 L of oxygen at a pressure of 2×10^{-6} Torr and subsequent annealing at 400 °C for 5 min. *In situ* photoelectron spectroscopy was then carried out in the same UHV chamber using the synchrotron radiation at BESSY II, Berlin, Germany. Using the high flux undulator beamline UE56/2-PGM1 at 600 eV photon energy, the XPS spectra were continuously recorded during the metal evaporation. Before and after evaporation, high-resolution scans of the carbon 1s, silicon 2p, and the metal photoelectron core levels were taken. The core level spectra were then fitted using nonlinear least-squares line shape analysis after subtraction of a Shirley background. For the graphene contribution to the C 1s core level a Doniach−Sunjic line shape is used, while all other contributions were fitted using a Voigt line shape. The core level spectra taken directly before evaporation are in excellent agreement with spectra shown by Riedl *et al.*[46] and Speck *et al.*[47] for quasi-freestanding monolayer graphene and the survey spectrum shows no contamination of the graphene surface with oxygen, while the C 1s core level also shows no contamination with hydrocarbons. Apart from the Si 2p, the Si 2s, and the C 1s core levels, no additional contamination-related core levels were observed.

DFT Simulation. We use density functional theory implemented within the Quantum-ESPRESSO *ab initio* software package.[58] Electron exchange and correlation effects are described using the generalized-gradient corrected Perdew−Burke−Ernzerhof (PBE) approximation.[49] Ion cores are treated using ultrasoft (Vanderbilt) pseudopotentials.[59] Periodic boundary conditions were used in all three dimensions using a hexagonal unit cell, which contains eight carbon atoms and 18 metal atoms. Fermi−Dirac smearing was used with a smearing width of 0.086 eV. A fixed lattice constant (c_{lat}) of 30 Å was used in the *z*-direction to create a vacuum layer to prevent periodic images from interacting with each other. We construct a supercell arrangement of Ti atoms on graphene shown in Figure 5a that is consistent with the orientation from the TEM experiments. Six metal atom layers are used, corresponding to a ~1.2 nm thick slab of metal on graphene. A similar arrangement of Pd atoms, in Figure 5b, is also considered which corresponds to the Pd(111) surface with cubic symmetry *ABCABC* stacking as opposed to hexagonal symmetry *ABABAB* stacking for Ti(0001). In addition, we also constructed a Pd(110) orientation surface shown in Figure 5c, which consists of five layers to match our TEM data. The electronic wave function is expanded in a plane wave basis set with an energy cutoff of 60 Ry and a charge density cutoff of 500 Ry. Brillouin zone sampling was done using a Monkhorst−Pack mesh[60] of 8 × 8 × 1. Total energies for the adsorption energy were calculated for optimized lattice parameters for graphene, the metal slab, and the graphene−metal complex. All cell optimizations were performed using a force convergence threshold of 3×10^{-4} Ry/a_0. Initial geometries for cell optimizations began with metallic layers ~2 Å or less above graphene and relaxed to the final optimized height. A supercell of Pd[110] on graphene was created by recognizing that a 3 × 2 supercell created from an orthorhombic unit cell for Pd[110] had very similar lattice matching to a 2 × 3 supercell created from an

orthorhombic unit cell of graphene. This Pd−graphene complex consists of five layers, containing 24 carbon atoms and 30 Pd atoms, and was optimized such that no stress acted on the cell. DFT calculations for this system were performed using GGA/PBE, Vanderbilt ultrasoft pseudopotential, 60 Ryd planewave cutoff, 500 Ryd charge density cutoff, Fermi−Dirac smearing with a smearing width of 0.086 eV, and a Monkhorst−Pack mesh of $4 \times 4 \times 1$.

Larger scale structure search calculations assuming metal clusters could shed light on this possibility in the future. These results may also be influenced by the use of the generalized gradient approximation (GGA)/PBE exchange correlation functional. van der Waals functional (vdW-DF) studies and RPA-based studies of metal adsorption on graphene have been performed that suggest the GGA/PBE approach under binds physisorbed metals by up to several tens of meV.[61−63] Therefore, the relative energies of the Pd(111) and Pd(110) surface binding may be sensitive to the choice of exchange and correlation approach. We also performed LDA and included van der Waals corrections (DFT-D) for dispersion interactions (shown in Table S1, Supporting Information) and still found that Ti is still predicted to bind more favorably to graphene than Pd(111). Even inclusion of van der Waals corrections or using LDA for 6L−Pd(111) still shows little p−d hybridization (see the Supporting Information).

Conflict of Interest: The authors declare no competing financial interest.

Supporting Information Available: Additional information with regard to the calculation of adhesion energy, Raman spectra of titanium + QFMLG and various deposition conditions, HR-TEM of titanium lattice constant, Ni and Au SAED, and van der Waals corrections. This material is available free of charge *via* the Internet at http://pubs.acs.org.

Acknowledgment. This work has been partially funded by the MSD MARCO program, the Army−MIT Institute for Soldier Nanotechnology, the Army Research Laboratory, and the ONR GATE MURI program. K.K.K. and J.K. acknowledge funding from the National Science Foundation (NSF) DMR 0845358. T.S. and R.K. acknowledge funding by the DFG in the framework of SFB 953 Synthetic Carbon Allotropes, W. Mahler and B. Zada for support during beamtime, the Helmholtz Zentrum Berlin for travel support, and K. Horn for providing access to his photoemission setup.

REFERENCES AND NOTES

1. Bolotin, K.; Sikes, K.; Jiang, Z.; Klima, M.; Fudenberg, G.; Hone, J.; Kim, P.; Stormer, H. Ultrahigh Electron Mobility in Suspended Graphene. *Solid State Commun.* **2008**, *146*, 351–355.
2. Balandin, A. A.; Ghosh, S.; Bao, W.; Calizo, I.; Teweldebrhan, D.; Miao, F.; Lau, C. N. Superior Thermal Conductivity of Single-Layer Graphene. *Nano Lett.* **2008**, *8*, 902–907.
3. Lee, C.; Wei, X.; Kysar, J. W.; Hone, J. Measurement of the Elastic Properties and Intrinsic Strength of Monolayer Graphene. *Science* **2008**, *321*, 385–388.
4. Chen, S.; Brown, L.; Levendorf, M.; Cai, W.; Ju, S.-Y.; Edgeworth, J.; Li, X.; Magnuson, C. W.; Velamakanni, A.; Piner, R. D.; et al. Oxidation Resistance of Graphene-Coated Cu and Cu/Ni Alloy. *ACS Nano* **2011**, *5*, 1321–1327.
5. Bonaccorso, F.; Sun, Z.; Hasan, T.; Ferrari, A. C. Graphene Photonics and Optoelectronics. *Nat. Photonics* **2010**, *4*, 611–622.
6. Dankerl, M.; Hauf, M. V.; Lippert, A.; Hess, L. H.; Birner, S.; Sharp, I. D.; Mahmood, A.; Mallet, P.; Veuillen, J.-Y.; Stutzmann, M.; et al. Graphene Solution-Gated Field-Effect Transistor Array for Sensing Applications. *Adv. Funct. Mater.* **2010**, *20*, 3117–3124.
7. Palacios, T.; Hsu, A.; Wang, H. Applications of Graphene Devices in RF Communications. *IEEE Commun. Mag.* **2010**, *48*, 122–128.
8. Pop, E.; Varshney, V.; Roy, A. K. Thermal Properties of Graphene: Fundamentals and Applications. *MRS Bull.* **2012**, *37*, 1273–1281.
9. Jenkins, K. A.; Farmer, D. B.; Avouris, P.; Valdes-Garcia, A.; Dual-Gate Graphene, FETs With fT of 50 GHz. *IEEE Electron Device Lett.* **2010**, *31*, 68–70.
10. Wu, Y.; Lin, Y.-M.; Bol, A. A.; Jenkins, K. A.; Xia, F.; Farmer, D. B.; Zhu, Y.; Avouris, P. High-Frequency, Scaled Graphene Transistors on Diamond-like Carbon. *Nature* **2011**, *472*, 74–78.
11. Chen, C.; Rosenblatt, S.; Bolotin, K. I.; Kalb, W.; Kim, P.; Kymissis, I.; Stormer, H. L.; Heinz, T. F.; Hone, J. Performance of Monolayer Graphene Nanomechanical Resonators with Electrical Readout. *Nat. Nano* **2009**, *4*, 861–867.
12. Dean, C. R.; Young, A. F.; Meric, I.; Lee, C.; Wang, L.; Sorgenfrei, S.; Watanabe, K.; Taniguchi, T.; Kim, P.; Shepard, K. L.; et al. Boron Nitride Substrates for High-Quality Graphene Electronics. *Nat. Nanotechnol.* **2010**, *5*, 722–726.
13. Russo, S.; Craciun, M. F.; Yamamoto, M.; Morpurgo, A. F.; Tarucha, S. Contact Resistance in Graphene-Based Devices. *Phys. E Low-Dimens. Syst. Nanostruct.* **2010**, *42*, 677–679.
14. Venugopal, A.; Colombo, L.; Vogel, E. M. Contact Resistance in Few and Multilayer Graphene Devices. *Appl. Phys. Lett.* **2010**, *96*, 013512.
15. Vo-Van, C.; Kassir-Bodon, Z.; Yang, H.; Coraux, J.; Vogel, J.; Pizzini, S.; Bayle-Guillemaud, P.; Chshiev, M.; Ranno, L.; Guisset, V.; et al. Ultrathin Epitaxial Cobalt Films on Graphene for Spintronic Investigations and Applications. *New J. Phys.* **2010**, *12*, 103040.
16. Byon, H. R.; Suntivich, J.; Shao-Horn, Y. Graphene-Based Non-Noble-Metal Catalysts for Oxygen Reduction Reaction in Acid. *Chem. Mater.* **2011**, *23*, 110718132807038.
17. Chung, K.; Lee, C.-H.; Yi, G.-C. Transferable GaN Layers Grown on ZnO-Coated Graphene Layers for Optoelectronic Devices. *Science* **2010**, *330*, 655–657.
18. Profeta, G.; Calandra, M.; Mauri, F. Phonon-Mediated Superconductivity in Graphene by Lithium Deposition. *Nat. Phys.* **2012**, *8*, 131–134.
19. Han, M.; Özyilmaz, B.; Zhang, Y.; Kim, P. Energy Band-Gap Engineering of Graphene Nanoribbons. *Phys. Rev. Lett.* **2007**, 98.
20. Nair, R. R.; Ren, W.; Jalil, R.; Riaz, I.; Kravets, V. G.; Britnell, L.; Blake, P.; Schedin, F.; Mayorov, A. S.; Yuan, S.; et al. Fluorographene: A Two-Dimensional Counterpart of Teflon. *Small* **2010**, *6*, 2877–2884.
21. Elias, D. C.; Nair, R. R.; Mohiuddin, T. M. G.; Morozov, S. V.; Blake, P.; Halsall, M. P.; Ferrari, A. C.; Boukhvalov, D. W.; Katsnelson, M. I.; Geim, A. K.; et al. Control of Graphene's Properties by Reversible Hydrogenation: Evidence for Graphane. *Science* **2009**, *323*, 610–613.
22. Gao, L.; Guest, J. R.; Guisinger, N. P. Epitaxial Graphene on Cu(111). *Nano Lett.* **2010**, *10*, 3512–3516.
23. Sutter, P. W.; Flege, J.-I.; Sutter, E. A. Epitaxial Graphene on Ruthenium. *Nat. Mater.* **2008**, *7*, 406–411.
24. Wofford, J. M.; Starodub, E.; Walter, A. L.; Nie, S.; Bostwick, A.; Bartelt, N. C.; Thürmer, K.; Rotenberg, E.; McCarty, K. F.; Dubon, O. D. Extraordinary Epitaxial Alignment of Graphene Islands on Au(111). arXiv:1202.0561, **2012**.
25. Kralj, M.; Pletikosić, I.; Petrović, M.; Pervan, P.; Milun, M.; N'Diaye, A. T.; Busse, C.; Michely, T.; Fujii, J.; Vobornik, I. Graphene on Ir(111) Characterized by Angle-Resolved Photoemission. *Phys. Rev. B* **2011**, *84*, 075427.
26. Varykhalov, A.; Sánchez-Barriga, J.; Shikin, A. M.; Biswas, C.; Vescovo, E.; Rybkin, A.; Marchenko, D.; Rader, O. Electronic and Magnetic Properties of Quasifreestanding Graphene on Ni. *Phys. Rev. Lett.* **2008**, *101*, 157601.
27. Varykhalov, A.; Marchenko, D.; Sánchez-Barriga, J.; Scholz, M. R.; Verberck, B.; Trauzettel, B.; Wehling, T. O.; Carbone, C.; Rader, O. Intact Dirac Cones at Broken Sublattice Symmetry: Photoemission Study of Graphene on Ni and Co. *Phys. Rev. X* **2012**, *2*, 041017.
28. Wang, W. X.; Liang, S. H.; Yu, T.; Li, D. H.; Li, Y. B.; Han, X. F. The Study of Interaction between Graphene and Metals by Raman Spectroscopy. *J. Appl. Phys.* **2011**, *109*, 07C501–07C503.
29. Sundaram, R. S.; Steiner, M.; Chiu, H.-Y.; Engel, M.; Bol, A. A.; Krupke, R.; Burghard, M.; Kern, K.; Avouris, P. The Graphene−Gold Interface and Its Implications for Nanoelectronics. *Nano Lett.* **2011**, *11*, 3833–3837.

30. Pi, K.; McCreary, K. M.; Bao, W.; Han, W.; Chiang, Y. F.; Li, Y.; Tsai, S.-W.; Lau, C. N.; Kawakami, R. K. Electronic Doping and Scattering by Transition Metals on Graphene. *Phys. Rev. B* **2009**, *80*, 075406.
31. Gallium Nitride Grown on Graphene. *Science* **2010**, *330*, 556−556.
32. Li, X.; Cai, W.; An, J.; Kim, S.; Nah, J.; Yang, D.; Piner, R.; Velamakanni, A.; Jung, I.; Tutuc, E.; et al. Large-Area Synthesis of High-Quality and Uniform Graphene Films on Copper Foils. *Science* **2009**, *324*, 1312–1314.
33. Kim, S.; Nah, J.; Jo, I.; Shahrjerdi, D.; Colombo, L.; Yao, Z.; Tutuc, E.; Banerjee, S. K. Realization of a High Mobility Dual-Gated Graphene Field-Effect Transistor with Al2O3 Dielectric. *Appl. Phys. Lett.* **2009**, *94*, 062107.
34. Iqbal, M. W.; Singh, A. K.; Iqbal, M. Z.; Eom, J. Raman Fingerprint of Doping due to Metal Adsorbates on Graphene. *J. Phys.: Condens. Matter* **2012**, *24*, 335301.
35. Mohiuddin, T. M. G.; Lombardo, A.; Nair, R. R.; Bonetti, A.; Savini, G.; Jalil, R.; Bonini, N.; Basko, D. M.; Galiotis, C.; Marzari, N.; et al. Uniaxial Strain in Graphene by Raman Spectroscopy: G Peak Splitting, Grüneisen Parameters, and Sample Orientation. *Phys. Rev. B* **2009**, *79*, 205433.
36. Hsu, A.; Wang, H.; Kim, K. K.; Kong, J.; Palacios, T. Impact of Graphene Interface Quality on Contact Resistance and RF Device Performance. *IEEE Electron Device Lett.* **2011**, *32*, 1008–1010.
37. Casiraghi, C. Doping Dependence of the Raman Peaks Intensity of Graphene close to the Dirac Point. *Phys. Rev. B* **2009**, *80*.
38. Howard, C. A.; Dean, M. P. M.; Withers, F. Phonons in Potassium-Doped Graphene: The Effects of Electron-Phonon Interactions, Dimensionality, and Adatom Ordering. *Phys. Rev. B* **2011**, *84*, 241404.
39. Khomyakov, P. A.; Giovannetti, G.; Rusu, P. C.; Brocks, G.; van den Brink, J.; Kelly, P. J. First-Principles Study of the Interaction and Charge Transfer between Graphene and Metals. *Phys. Rev. B* **2009**, *79*, 195425.
40. Venezuela, P.; Lazzeri, M.; Mauri, F. Theory of Double-Resonant Raman Spectra in Graphene: Intensity and Line Shape of Defect-Induced and Two-Phonon Bands. *Phys. Rev. B* **2011**, *84*, 035433.
41. Chacón-Torres, J. C.; Pichler, T. Defect Modulated Raman Response of KC8 Single Crystals. *Phys. Status Solidi B* **2011**, *248*, 2744–2747.
42. Ferrari, A. C.; Meyer, J. C.; Scardaci, V.; Casiraghi, C.; Lazzeri, M.; Mauri, F.; Piscanec, S.; Jiang, D.; Novoselov, K. S.; Roth, S.; et al. Raman Spectrum of Graphene and Graphene Layers. *Phys. Rev. Lett.* **2006**, *97*, 187401.
43. Andrea, C.; Raman, F. Spectroscopy of Graphene and Graphite: Disorder, Electron−phonon Coupling, Doping and Nonadiabatic Effects. *Solid State Commun.* **2007**, *143*, 47–57.
44. Zhou, Q.; Coh, S.; Cohen, M. L.; Louie, S. G.; Zettl, A. Imprint of Transition Metal D Orbitals on a Graphene Dirac Cone. *Phys. Rev. B* **2013**, *88*, 235431.
45. Gong, C.; Lee, G.; Shan, B.; Vogel, E. M.; Wallace, R. M.; Cho, K. First-Principles Study of Metal−graphene Interfaces. *J. Appl. Phys.* **2010**, *108*, 123711–123711−8.
46. Riedl, C.; Coletti, C.; Iwasaki, T.; Zakharov, A. A.; Starke, U. Quasi-Free-Standing Epitaxial Graphene on SiC Obtained by Hydrogen Intercalation. *Phys. Rev. Lett.* **2009**, *103*, 246804.
47. Speck, F.; Ostler, M.; Röhrl, J.; Jobst, J.; Waldmann, D.; Hundhausen, M.; Ley, L.; Weber, H. B.; Seyller, Th. Quasi-Freestanding Graphene on SiC(0001). *Mater. Sci. Forum* **2010**, *645−648*, 629–632.
48. Gong, C.; McDonnell, S.; Qin, X.; Azcatl, A.; Dong, H.; Chabal, Y. J.; Cho, K.; Wallace, R. M. Realistic Metal−Graphene Contact Structures. *ACS Nano* **2014**, *8*, 642–649.
49. Perdew, J. P.; Burke, K.; Ernzerhof, M. Generalized Gradient Approximation Made Simple. *Phys. Rev. Lett.* **1996**, *77*, 3865–3868.
50. Bonn, D.; Eggers, J.; Indekeu, J.; Meunier, J.; Rolley, E. Wetting and Spreading. *Rev. Mod. Phys.* **2009**, *81*, 739–805.
51. Taur, Y.; Sun, J. Y.-C.; Moy, D.; Wang, L. K.; Davari, B.; Klepner, S. P. Source-Drain Contact Resistance in CMOS with Self-Aligned TiSi2. *IEEE Trans. Electron Devices* **1987**, *34*, 575–580.
52. Wang, Y.; Gong, Y.; Zheng, X.; Zhou, M. End-on *versus* Side-on Coordination of Dinitrogen to Titanium−benzene Complex. *Chem. Phys. Lett.* **2006**, *431*, 13–18.
53. Li, B.; Zhou, L.; Wu, D.; Peng, H.; Yan, K.; Zhou, Y.; Liu, Z. Photochemical Chlorination of Graphene. *ACS Nano* **2011**, *5*, 5957–5961.
54. Robinson, J. T.; Burgess, J. S.; Junkermeier, C. E.; Badescu, S. C.; Reinecke, T. L.; Perkins, F. K.; Zalalutdniov, M. K.; Baldwin, J. W.; Culbertson, J. C.; Sheehan, P. E.; et al. Properties of Fluorinated Graphene Films. *Nano Lett.* **2010**, *10*, 3001–3005.
55. Matsubayashi, A.; Abel, J.; Sinha, D. P.; Lee, J. U.; LaBella, V. P. Growth and Characterization of Metal Oxides Layers on CVD Graphene. *Bull. Am. Phys. Soc.* **2012**, *57*(1).
56. Regan, W.; Alem, N.; Alemán, B.; Geng, B.; Girit, Ç.; Maserati, L.; Wang, F.; Crommie, M.; Zettl, A. A Direct Transfer of Layer-Area Graphene. *Appl. Phys. Lett.* **2010**, *96*, 113102.
57. Emtsev, K. V.; Bostwick, A.; Horn, K.; Jobst, J.; Kellogg, G. L.; Ley, L.; McChesney, J. L.; Ohta, T.; Reshanov, S. A.; R|[ouml]|hrl, J.; et al. Towards Wafer-Size Graphene Layers by Atmospheric Pressure Graphitization of Silicon Carbide. *Nat. Mater.* **2009**, *8*, 203–207.
58. Giannozzi, P.; Baroni, S.; Bonini, N.; Calandra, M.; Car, R.; Cavazzoni, C.; Ceresoli, D.; Chiarotti, G. L.; Cococcioni, M.; Dabo, I.; et al. QUANTUM ESPRESSO: A Modular and Open-Source Software Project for Quantum Simulations of Materials. *J. Phys.: Condens. Matter* **2009**, *21*, 395502.
59. Vanderbilt, D. Soft Self-Consistent Pseudopotentials in a Generalized Eigenvalue Formalism. *Phys. Rev. B* **1990**, *41*, 7892–7895.
60. Monkhorst, H. J.; Pack, J. D. Special Points for Brillouin-Zone Integrations. *Phys. Rev. B* **1976**, *13*, 5188–5192.
61. Vanin, M.; Mortensen, J. J.; Kelkkanen, A. K.; Garcia-Lastra, J. M.; Thygesen, K. S.; Jacobsen, K. W. Graphene on Metals: A van Der Waals Density Functional Study. *Phys. Rev. B* **2010**, *81*, 081408.
62. Olsen, T.; Thygesen, K. S. Random Phase Approximation Applied to Solids, Molecules, and Graphene-Metal Interfaces: From van Der Waals to Covalent Bonding. *Phys. Rev. B* **2013**, *87*, 075111.
63. Olsen, T.; Yan, J.; Mortensen, J. J.; Thygesen, K. S. Dispersive and Covalent Interactions between Graphene and Metal Surfaces from the Random Phase Approximation. *Phys. Rev. Lett.* **2011**, *107*, 156401.